Plasmonic/magnetic molybdenum trioxide and graphitic carbon nitride quantum dots-based fluoroimmunosensing system for influenza virus

Plasmonic/magnetic molybdenum trioxide and graphitic carbon nitride quantum dots-based fluoroimmunosensing system for influenza virus

Ojodomo J. Achadu[a], Kenshin Takemura[b], Indra Memdi Khoris[b], Enoch Y. Park[a,b,*]

[a] *Research Institute of Green Science and Technology, Shizuoka University, 836 Ohya Suruga-ku, Shizuoka 422-8529, Japan*

[b] *Laboratory of Biotechnology, Department of Bioscience, Graduate School of Science and Technology, Shizuoka University, 836 Ohya Suruga-ku, Shizuoka 422-8529, Japan*

E-mail:
ojodomo.john.achadu@shizuoka.ac.jp (OJA)
takemura.kenshin.16@shizuoka.ac.jp (KT)
indra.memdi.khoris.17@shizuoka.ac.jp (IMK)
park.enoch@shizuoka.ac.jp (EYP)

* Corresponding author:
  E-mail address: park.enoch@shizuoka.ac.jp (E.Y. Park). Tel (Fax): +81-54-238-4887

21 **ABSTRACT**

22 A novel magnetic/plasmonic-assisted fluoro-immunoassay system is developed

23 for the detection of influenza virus using magnetic-derivatized plasmonic

24 molybdenum trioxide quantum dots (MP-MoO$_3$ QDs) as the plasmonic/magnetic

25 agent and fluorescent graphitic carbon nitride quantum dots (gCNQDs) as the

26 monitoring probe. Specific antibody against influenza A virus was conjugated

27 onto the surface of MP-MoO$_3$ QDs and gCNQDs, respectively. In the presence of

28 influenza A virus (as the test virus), a core-satellite immunocomplex is formed

29 between the antibody-conjugated nanomaterials (Ab-MP-MoO$_3$ QDs and Ab-

30 gCNQDs) and their interaction resulted in the modulation and gradual

31 enhancement of the fluorescence intensity of the detection probe with the

32 influenza virus concentration-dependent increase. In addition, PL change without

33 influenza A virus was not observed. Limits of detection of 0.25 and 0.9 pg/mL

34 were achieved for Influenza virus A/New Caledonia (20/99/IVR/116) (H1N1)

35 detection in deionized water and human serum, respectively. Clinically isolated

36 influenza virus A/Yokohama (110/2009) (H3N2) was detected in the range of 45

37 – 25,000 PFU/mL, with a limit of detection ca 45 PFU/mL (as opposed to a

38 minimum of 5000 PFU/mL for a commercial test kit). This developed biosensor

39 provides a robust, sensitive as well as a selective platform for influenza virus

40 detection. ***Keywords:*** Graphitic carbon nitride QDs; Magnetoplasmonic

41 molybdenum trioxide QDs; Influenza virus; Fluoroimmunosensing; Localized

42 surface plasmonic resonance.

1. Introduction

The recent outbreak of a novel coronavirus disease (COVID-19) and its potential for adverse effect on the global economy is an example of how quickly new infectious diseases can arise and spread [1]. Outbreaks such as this can unexpectedly cause demands for clinical knowledge, rapid diagnostic strategies, and epidemiological studies before a pandemic occurs. The rapid and ultrasensitive detection of infectious diseases is critical for the prevention and/or control of outbreaks. Therefore, it is crucial to continually deploy innovative materials to further develop the practical applications of biosensing systems capable of detecting biomolecules (DNAs, RNAs, proteins and virus particles) and of diagnozing other potentially harmful infectious diseases.

The deployment of carbon-based quantum dots as optical probes has received a tremendous boost due to their excellent optical properties, biocompatibility and low cost of preparation [2–7]. As carbon-based nanomaterials, graphitic carbon nitrides QDs (gCNQDs) possess excellent optical properties comparable to traditional heavy metal-based QDs, and are not as toxic. So, they are becoming competitive materials in nanosensors development [8–11]. The presence of graphitic nitride-N-atoms introduces a different kind of "surface state" which impacts some semiconductor-like properties [12–14]. This feature has attractively bestowed an edge on gCNQDs and their derivatives for utilization in optical and electrochemical-based sensing [15, 16]. For instance, a robust photo-electrochemical immunosensor was designed by Sun et al. for the sensitive detection of avian viruses using hybrid of gold nanoparticles (AuNPs)

66 and gCNQDs coupled to CdTe QDs [10]. Wang et al. reported a photo-

67 electrochemical platform for methylated RNA detection using gCNQDs/CdS

68 hybrid [17]. Pang et al. reported the fabrication of pcDNA3-HBV nanobiosensor

69 using gCNQDs-sensitized TiO_2 nanopillars [9]. Interestingly, the tailored surface

70 modification of gCNQDs has been achieved with moieties that acted as receptors

71 to capture and detect target analytes. In our previous work, the surface of

72 gCNQDs was functionalized with 2, 2, 6, 6-tetramethyl (piperidin-1-yl) oxyl

73 (TEMPO) to detect ascorbic acid in the presence of zinc phthalocyanine [2].

74 Furthermore, biomolecules including thymine and tannic acid have been grafted

75 onto the surface gCNQDs for the purpose of deriving Hg^{2+}, Cu^{2+} and ascorbic

76 acid responsive nanosensors, respectively [18, 19].

77   On the other hand, novel materials which can serve as viable alternatives

78 to Au and Ag are desired and are a hotspot for research [20, 21]. This is due in

79 large part to the high cost of preparation and/or procurement of noble metals

80 nanoparticles (NPs). As a result, a new low-cost, easy-to-prepare and non-toxic

81 molybdenum trioxide QDs (MoO_3 QDs) with excellent plasmonic properties are

82 gaining traction [21–28]. MoO_3 QDs are few-crystalline-structured nanoparticles

83 with single-layered morphology and oxygen vacancies. Hence, they exhibit a

84 semiconductor-based tunable localized surface plasmonic resonance (LSPR),

85 comparable to noble metals NPs, both in the visible and near-infrared (NIR)

86 regions [27, 28]. To demonstrate that the inherent tunable LSPR of MoO_3 QDs

87 can be harnessed for opto-electrical sensing, MoO_3 QDs was adopted as a

88 substrate for the surface enhanced Raman spectroscopy (SERS) detection of

89   bovine serum albumin (BSA) and methylene blue (MB), respectively. The Raman

90   signals of the probe molecule (Rhodamine 6G) and MB were strongly amplified

91   due to the interfacial charge transfer effect between the substrates and probe

92   molecule. The intense LSPR absorption of MoO_3 QDs in the near infrared (NIR)

93   region was deployed in the photothermal ablation of cancer, glucose detection

94   in the fluorescence (FL)-based detection of 2, 4, 6-trinitrotoluene (TNT) [23, 25].

95   Plasmonic nanostructures are known to influence the fluorescence (FL)

96   properties of QDs via plasmon-induced energy transfer [29, 30]. Optical

97   biosensing platforms have been designed based on this kind of interaction [31,

98   35]. For the first time, we have synthesized novel, water-soluble

99   magnetoplasmonic MoO_3 QDs and examined their potential as a plasmonic

100 material in the presence of gCNQDs for ultrasensitive FL signal enhancement-

101 based assay to detect extremely low concentrations of influenza virus A (H1N1)

102 and (H3N2) RNAs. The use of gCNQDs/MP-MoO_3 QDs as a novel and

103 interesting combination of functional materials for optical biosensing was

104 inspired by the high FL of gCNQDs, the strong plasmonic effect of MP-MoO_3

105 QDs, their intrinsic non-toxicity and the desire to fabricate low-cost biosensing

106 systems. As a result, a simple and sensitive fluoroimmunoassay of influenza virus

107 was developed using hybrid combination of gCNQDs and MP-MoO_3 QDs. The

108 detection principle was based on the antigen-antibody interaction achieved

109 between the immunocomplex of antibody-conjugated gCNQDs and MP-MoO_3

110 QDs, respectively. The detection protocol maintained a magnetic separation and

111 purification of the target influenza virus from complex matrices and impurities

owing to the magnetic functionality of the MoO$_3$ QDs which was another extremely useful feature apart from plasmonic effects. This was intended to optimize the FL signal enhancement of the probe QDs. This step, as expected, resulted in a signal enhancement and sensitivity of the established immunoassay. The target influenza virus was separated easily by an external magnet field allowing an ultrasensitive detection of influenza virus A (H1N1) and clinically isolated influenza virus A (H3N2) RNA, respectively. The biosensing system has been developed to provide a robust performance, as well as high selectivity and ultrasensitivity for influenza virus detection when compared to a commercially available rapid influenza diagnostic test (RIDT) kits.

2. Materials and methods

2.1. Materials

Melamine, glutaraldehyde, citric acid (CA), dimethyl formamide (DMF), iron (II) chloride, iron (III) chloride, bovine serum albumin (BSA), N-hydroxysuccinimide (NHS), and N-(3-dimethylaminopropyl)-N'-ethylcarbodiimide hydrochloride (EDC) were purchased from Sigma-Aldrich (St Louis, USA). Polyvinylpyrrolidone (PVP), ammonium molybdate tetra-hydrate were supplied by Wako Pure Chemicals Ind. (Osaka, Japan).

Anti-human influenza A (H1N1) monoclonal antibody (clone C179), anti-human influenza A (H3N2) monoclonal antibody (Clone F49) and anti-human

influenza A (H1, H2, H3) monoclonal antibody (Clone C111) which is positive for both influenza viruses H1N1 and H3N2 was purchased from Takara Bio. Inc, (Kusatsu, Shiga, Japan). Influenza virus A/New Caledonia (20/99/IVR/116) (H1N1) was purchased from ProSpec-Tany TechnoGene Ltd. (Rehovot, Israel). Clinically isolated influenza virus A/Yokohama/110/2009 (H3N2) was kindly provided by Dr. C. Kawakami of Yokohama City Institute of Health, Japan. Goat anti-rabbit IgG-HRP were purchased from Santa Cruz Biotechnology (Dallas, Texas, USA). Commercial RIDT kit - *QuikNavi Flu 2* was purchased from Denka - Seiken Co. Ltd. (Tokyo, Japan). Zika virus was kindly provided by Prof. K. Morita of Institute of Tropical Medicine, Nagasaki University. Noro virus-like particles (NoV-LPs) were prepared in our lab according to previously reported protocol [36]. HEV-LPs were prepared according to Li et al. [37]. All experiments were carried out using high purity deionized (DI) water (>18 MΩ·cm).

2.2. Equipment

Ground state electronic absorption (UV/Vis), fluorescence excitation and emission spectra were recorded on a filter-based multimode microplate reader (Infinite F200 M; TECAN, Ltd, Männedorf, Switzerland). Images of transmission electron microscope (TEM) and scanning electron micrograph (SEM) were obtained using JEM-2100F (JEOL, Ltd., Tokyo, Japan) operating at 100 kV and 200 kV, respectively. The morphological and structural characteristics of

155 gCNQDs were also obtained using a high resolution transmission electron

156 microscope (HRTEM) coupled with a JEOL 2010 TEM operating at an

157 accelerating electrical potential of 200 kV.

158   Atomic force microscopy (AFM) measurement in tapping mode was

159 carried out with MFP-3D Origin supplied by Asylum research (Oxford

160 instruments company, USA). AFM analysis was done by drop casting and room

161 temperature drying of the samples solutions on a freshly cleaved mica surface.

162 Dynamic light scattering (DLS) and zeta potential experiments were done on a

163 Malvern Zetasizer nanoseries, Nano-ZS90 (Malvern Inst. Ltd., Malvern, UK).

164 Powder X-ray diffraction (PXRD) analysis was carried out using a RINT ULTIMA

165 XRD (Rigaku Co., Tokyo, Japan) with αNi filter and a Cu-Kα source. Data were

166 collected over $2\theta = 30 - 90°$ at a scan rate of 0.01°/step and 10 s/point. Fourier

167 transform infrared spectroscopy was performed using FT/IR-6300 with ATR

168 PRO610P-S (JASCO, Tokyo, Japan). Raman spectroscopic measurements were

169 carried out using NRS-7100 Raman Spectrometer with f500 spectrograph (JASCO,

170 Tokyo, Japan). Conjugation of the antibody to the respective QDs and

171 nanoparticles was confirmed by enzyme-linked immunosorbent assay (ELISA)

172 using a microplate (Model 680; Bio-Rad, Hercules, USA).

173

174 *2.3. Synthesis of graphitic carbon nitride QDs (gCNQDs)*

175 Melamine was used to synthesize graphitic carbon nitride nanosheets (gCNNs)

176 according to reported procedures [38]. Graphitic carbon nitride QDs (gCNQDs)

177 were prepared by the solvothermal treatment of the graphitic nanosheets

178 (gCNNs) according to previously reported method with modifications [18].

179 Briefly, gCNNs (0.1 g) and citric acid (0.2 g) were dissolved in 10 mL of DMF,

180 stirred for 5 min and sonicated for 20 min to obtain homogenous suspension.

181 The suspension was transferred and sealed in a 50 mL Teflon-lined stainless steel

182 autoclave and heated at 160°C for 12 h. The autoclave was allowed to cool to

183 room temperature naturally. The obtained product was filtered through a 0.22

184 μm microporous filter membrane and then dialyzed (using a membrane of

185 MWCO 1.5 kDA) for 48 h to obtain pure gCNQDs solution. The solution was

186 further freeze dried to obtained solid product.

187

188 *2.4. Synthesis of magnetoplasmonic molybdenum trioxide QDs (MP-MoO$_3$ QDs)*

189 Pristine MoO$_3$ QDs was prepared by a room temperature ultraviolent (UV)

190 irradiation method according to reported procedure [28]. The novel magnetic-

191 derivatized MP-MoO$_3$ QDs were synthesized under hydrothermal conditions. In

192 a typical experiment, 0.15 g (0.12 mmol) of ammonium molybdate tetrahydrate

193 was dissolved in 20 mL mixture of deionized water and HCl (9:1). Then 0.1 g of

194 PVP was added to the mixture and stirred vigorously. After 5 min, 1 mmol of

195 FeCl$_2$ was added and the mixture was subsequently irradiated under a 365 nm

196 UV light with constant stirring. A dark blue product of MoO$_3$ QDs was formed

197 after 30 min and was left for a total of 1 h. The product was centrifuged to

198 remove unreacted/excess PVP and dialyzed using a 2.0 kDA dialysis tubing

199 membrane. Next, 5 mmol of $FeCl_3$ was added to 10 mL of the obtained product

200 and transferred to a Teflon-line stainless steel autoclave and heated at 160°C for

201 4 h. Subsequently, the product was washed with ethanol by centrifugation and

202 further purified by magnetic separation. To surface functionalize the MP-MoO_3

203 QDs with carboxyl groups, 2 mL of glutaraldehyde was incubated with 2 mg of

204 MP-MoO_3 QDs in ethanol stirred for 12 h. The product was purified using

205 magnetic separation. All experiments were carried out using ultrapure DI water.

206

207 *2.5. Conjugation of antibodies to gCNQDs and MP-MoO₃ QDs*

208 Anti-human influenza virus A (H1N1) (Clone C179) or (H1, H2, H3) (Clone C111)

209 monoclonal antibody was conjugated to gCNQDs via the well-known EDC/NHS

210 covalent chemistry (Scheme 1A). Briefly, 100 μL of 0.1 M EDC was added to 2

211 mL of gCNQDs solution to activate the carboxylic groups on their surfaces. The

212 solution was stirred at ambient temperature for 30 min. Next, 100 μL of 0.1 M

213 NHS was added to the mixture and further stirred for ~15 min followed by the

214 addition of 5.1 μg/mL of the antibodies in PBS 7.6. The resulting mixtures were

215 then stirred for 8 h at 7°C. The Ab-conjugated gCNQDs were purified by

216 centrifugation (3000 × g, 5 min) and subsequently dissolved in 2 mL of ultrapure

217 water and stored in the refrigerator for further use. Anti-human influenza virus A

218 (H1N1) monoclonal antibody (Clone C179) was conjugated to MP-MoO_3 QDs

following the above described procedures for the detection of influenza virus
A/New Caledonia/20/99/IVR/116 (H1N1) as shown in Scheme 1B. Anti-human
influenza virus A (H3N2) monoclonal antibody (Clone F49) was conjugated to
MP-MoO$_3$ QDs for the detection of the clinically isolated influenza virus
A/Yokohama/110/2009 (H3N2). The conjugation of antibodies (Ab) to gCNQDs
and MP-MoO$_3$ QDs, respectively, was confirmed using ELISA. Details have been
provided in our previous work [33].

2.6. Immunofluorescence detection of influenza virus (H1N1 or H3N2)

The respective antibody–conjugated gCNQDs and MP-MoO$_3$ QDs were used as
the detection probe (5% BSA was used for blocking to avoid non-specific
binding of the antibody-conjugated probes). Next, 50 µL of the probe solution
was placed in a 96-well plate, followed by the incubation of the respective
target influenza virus (20 µL) for 5 min before fluorescence measurements were
acquired. After the incubation duration, the antibody-antigen complex solutions
were excited at 500 nm, and the fluorescence spectra within the range of 530–
800 nm were recorded. The detection of influenza virus (H1N1) was carried out
in ultrapure water and human serum within the concentration range of 1 pg/mL
– 100 ng/mL. Clinically isolated H3N2 RNA was detected within the range of 45
– 25,000 PFU/mL. All detection experiments were done in triplicate. The limits
of detection (LODs) were evaluated by using $3\delta/K_0$, where δ is the standard

240 deviation of blank measurement (n=12) and K_0 is the slope of the generated

241 calibration curves following replicated measurements [39].

242

243 **3. Results and discussion**

244 *3.1. The design of the biosensing platform*

245 The oxygen-deficient MoO_3 nanostructures, like Au NPs, display intensive LSPR

246 absorption in the NIR-I region [27, 28]. The absorption spectra of MoO_3 QDs

247 strongly overlap with the FL spectra of gCNQDs (Fig. S1 in Supplementary data).

248 The beneficial NIR plasmonic absorption of MoO_3 QDs was therefore used in

249 enhancing the FL signal of gCNQDs via a plasmonic-induced energy transfer

250 process resulting from their close proximity in a core-satellite network triggered

251 by the "virus-antibody" affinity (Scheme 1C, D and Fig. S2 in Supplementary

252 data). In addition, MoO_3 QD's magnetic derivatization was extremely useful in

253 the purification the antibody-QDs conjugates produced and in the isolation of

254 the influenza antigens specifically captured, thus increasing the sensitivity of the

255 developed immunoassay. The immobilization of anti-influenza virus antibodies

256 on the surfaces of gCNQDs and MP-MoO_3 QDs ensured the successful and

257 precise binding of the antibody-conjugated materials to influenza virus. The

258 extent to which gCNQDs interact with MP-MoO_3 QDs to enable the plasmonic-

259 induced effect was dependent on influenza virus concentration. When the

260 concentration of influenza virus is increased, more plasmonic MP-MoO_3 QDs are

261 propelled closer to the fluorescent gCNQDs which triggered the spontaneous

262 enhancement in the FL of the gCNQDs.

263

264 *3.2. Structural/optical characterization of graphitic carbon nitride QDs*

265 In this work, bulk graphitic carbon nitride nanosheets (gCNNs) were treated

266 under solvothermal conditions to prepare highly fluorescent gCNQDs. In order

267 to characterize the prepared carbon-based QDs, various techniques ranging from

268 materials science to spectroscopy were employed. The transmission electron

269 microscopy (TEM) image obtained showed quasi-spherically shaped particles that

270 are monodispersed with size distribution between 5 – 9 nm (7.25±0.7 average

271 diameter) (Fig. 1A). The HRTEM image shows that the graphitic lattice spacing is

272 0.23 nm (Fig. 1A inset), which is a feature of the (002) hexagonal plane of

273 graphitic carbon nitrides [4, 8, 11]. The AFM results showed a narrow

274 distribution of the graphitic QDs with few layers of planar graphitic sheets having

275 nanoscopic size of ~5 nm with a height profile of 1.5 nm (Fig. 1B). The powder

276 X-ray diffraction (XRD) pattern (Fig. 1C) obtained for the prepared gCNQDs

277 exhibit a broad peak at 27.9° which corresponds to the graphitic interplanar 002

278 d-spacing which is known to be exhibited by graphitic QDs [8]. Chemical

279 functional groups were also elucidated by carrying out FTIR spectroscopy. In Fig.

280 1D, the spectra of gCNQDs displayed typical vibrations inherently possessed by

281 the precursors (gCNNs/CA). An intensely broad absorption was observed at

282 ~3688 – 2792 cm^{-1} which is due to the combined stretching vibrations of N-H

283 and O-H (from carboxyl group). The intense bands appearing at 1431, 1316 and

284 772 cm^{-1} are reminiscent of the stretching modes of C–C, C-N and breathing

285 mode of the s-triazine heterocycles characteristic of carbon nitrides [4, 8, 11]. The

286 C=O observed at 1625 cm^{-1} confirms the presence of carboxylic groups. To

287 complement the surface functional groups elucidation results obtained from FTIR

288 analysis, zeta potential analysis was performed in order to understand the

289 stability of the gCNQDs in solution and their surface chemistry. The results

290 obtained show that the zeta potential of the gCNQDs was -18.1 mV (Fig. S3A in

291 Supplementary data), which suggests that some carboxylic (COOH) functionality

292 are present on the gCNQDs surface. In comparison to some reported carbon

293 dots (CDs) and graphene QDs [40], the lower negative zeta potential value may

294 indicate the existence of amino (NH$_2$) and/or nitride functionality of the s-

295 triazine heterocycles expected to be associated with graphitic carbon nitride QDs

296 [41]. The result also shows that the gCNQDs may be dispersed in solution to a

297 moderate degree, as zeta potential values >20 mV are known to result in well-

298 dispersed colloidal solutions due to increased interparticle repulsion [40, 41].

299

300 The optical spectroscopy characterization of gCNQDs displayed a typical

301 strong ground-level absorption peak at ~542 nm and a broad absorption at <

302 500 nm (Fig. 2A). These absorptions are ascribed to the n-π^* and π-π^* electronic

303 transitions of the electron lone pairs of N atoms of s-triazine units [4, 8, 11, 18].

304 Further, the fluorescence properties of the as-synthesized gCNQDs were probed.

305 The FL emission of gCNQDs prepared under solvothermal conditions exhibit

306 emission extending into the yellow region with maximum fluorescence intensity

307 at 652 nm when excited at 500 nm wavelength (Fig. 2A). Carbon-based QDs

308 with similar fluorescence emission extending well into the red region have been

309 prepared using solvothermal processes [42, 43]. Another important parameter

310 evaluated for the prepared gCNQDs in terms of their suitability to function as an

311 optical probe is their fluorescence quantum yield (Φ_F). The robustness and

312 sensitivity of a given fluorescence-based material as a probe is dictated by

313 efficiently high Φ_F values. Interestingly, gCNQDs possess Φ_F of ~44%; using

314 Rhodamine 6G as the reference standard (see Supplementary Information for

315 details). It is plausible to infer that the presence of citric acid made the gCNQDs

316 water soluble (due to the incorporation of carboxylic group), and also created

317 additional defects/trap sites on the QDs surface (new surface states) [44, 45].

318 This probably may have resulted in an easy exciton mobility translating into such

319 a high Φ_F and red-shifted emission.

320

321 *3.3. Characterization of magnetoplasmonic MoO₃ QDs (MP-MoO₃ QDs)*

322 Novel magnetoplasmonic derivative of molybdenum-based QDs was prepared

323 in the presence of $FeCl_2$ and $FeCl_3$ as the magnetic component precursors. $FeCl_2$

324 was firstly reduced *in situ* by PVP and the subsequent hydrothermal treatment in

325 the presence of $FeCl_3$ ensured the surface grafting with magnetic NPs. Thanks to

326 the strong reducing and stabilizing properties of PVP, a dual role was played to

327 achieve the facile synthesis of MP-MoO$_3$ QDs hybrid. PVP acted as a surface

328 stabilizer/reducing agent for the magnetic NPs formation and initiated a strong

329 plasmonic resonance [28, 46]. Hence, the prepared MP-MoO$_3$ QDs manifested

330 an excellent aqueous solubility, stability and monodispersity. Optical

331 characterization revealed that the UV-vis absorption of the pristine MoO$_3$ QDs

332 and their magnetic derivative (MP-MoO$_3$ QDs) displayed LSPR peaks in the NIR

333 with a slight blue shift and peak broadening observed for the MP-MoO$_3$ QDs

334 (Fig. 2B). To probe the morphology of the MP-MoO$_3$ QDs, transmission electron

335 micrograph (TEM) images were acquired for the pristine MoO$_3$ QDs (without

336 magnetic NPs) and MP-MoO$_3$ QDs, respectively, (Fig. 3A and B). A relatively

337 narrow size distribution with near uniform shape was observed for MP-MoO$_3$

338 QDs with an average size of 13.2 ± 0.5 nm. The pristine MoO$_3$ QDs possess

339 average size of ~5 nm with a quasi-spherical morphology. Similar to TEM, a size

340 increase was observed in DLS analysis for the prepared hybrid. The mean

341 hydrodynamic diameter of the pristine MoO$_3$ QDs at ~3.2 nm was increased to

342 ~18 nm upon magnetic NPs functionalization (Fig. 3C). X-ray diffractogram

343 (XRD) patterns provided an insight into MP-MoO$_3$ QDs formation when

344 compared with the pattern of the pristine MoO$_3$ QDs. As shown in Fig, 3D,

345 pristine MoO$_3$ QDs are endowed with a broad peak within the range of 22 − 33°,

346 which shows that they have poor crystallinity [27, 28]. This peak has been

347 attributed to the (040) positions of a-MoO$_3$ (JCPDs no. 05-0508) [27].

348 Conversely, the MP-MoO$_3$ QDs hybrid displays the characteristic diffraction

349 pattern of MoO_3 QDs in 2θ range from $5-30°$ and that of magnetic constituent

350 at 2θ = 35°, 57° and 63° which corresponds to magnetic NPs marked indices of

351 (311), (511) and (440), respectively [47]. Energy dispersive X-ray spectroscopy

352 (EDX) was employed to elucidate the elemental compositions of MP-MoO_3 QDs.

353 The main compositional elements which are Mo and Fe are found as displayed

354 in the obtained spectra (Fig. 3E). The characteristic infrared absorptions which

355 have been assigned to Mo-O-Mo stretching vibrations in MoO_3 QDs were clearly

356 observed in the as-synthesized MP-MoO_3 QDs in the region within $500-885$

357 cm^{-1}. Mo=O stretching vibration was observed at 942 cm^{-1} (Fig. 3F) [27].

358 Vibrations corresponding to the moieties of PVP as the surface stabilizing agent

359 are further observed at 3169, 1644 and 1412 cm^{-1} (Fig. 3F). The acquired Raman

360 spectra for pristine MoO_3 QDs show the absorption typical of the Mo_3-O and

361 Mo_2-O vibrations at 776 and 820 cm^{-1}, respectively [27]. Compared to MP-

362 MoO_3 QDs, similar absorption occurred with the emergence of new peaks (Fig.

363 S4 in Supplementary data), possibly due to the surface functionalization with

364 magnetic NPs. These results indicate the successful preparation of the novel MP-

365 MoO_3 QDs nanocomposite. Further, the antibody conjugated MP-MoO_3 QDs

366 (Ab- MP-MoO_3 QDs) or Ab-gCNQDs were subjected to DLS analysis in order to

367 determine their hydrodynamic sizes. As shown in Fig. S5 (Supplementary data),

368 Ab-gCNQDs show an average hydrodynamic size increase from an average size

369 of ~7.5 nm to ~20 nm (Fig. S5A in Supplementary data). In a similar manner,

370 the size recorded for Ab-MP-MoO_3 QDs was ~24 nm showing some increase

371 from ~ 13 nm due to the antibody conjugation, Fig. S5B (Supplementary data),

372 thus confirming their functionalization, respectively.

373 *3.4. Magnetoplasmonic-amplified detection of influenza virus (H1N1)*

374 The virus detection protocol was established by using commercially obtained

375 pure influenza virus (H1N1). Human serum medium was used to mimic complex

376 biological media so as to demonstrate the applicability of the fabricated probe

377 for influenza virus detection in clinical samples. Thus, gCNQDs was deployed as

378 the fluorescent signal reporter and MP-MoO$_3$ QDs as the plasmonic and

379 magnetic material. MP-MoO$_3$ QDs induced a steady and gradual plasmonic-

380 induced enhancement of the FL of gCNQDs in the presence of increasing

381 concentrations of influenza virus (H1N1) in water and human serum, respectively

382 (Fig. 4A and B). The core-satellite immunocomplex formed between the Ab-

383 gCNQDs and Ab-MP-MoO$_3$ QDs can be easily isolated with a magnetic field

384 leading to sample concentration and an interference-free FL signal modulation.

385 The extent of the core-satellite immunocomplexing was directly proportional to

386 influenza virus (H1N1) concentration; this in turn led to stronger plasmonic

387 coupling effect as more MP-MoO$_3$ QDs are brought closer to the gCNQDs by the

388 antibody-antigen binding affinity. Consequently, corresponding linear calibration

389 curves were plotted to elucidate the linear dynamic detection range as shown in

390 Fig. 4C. The LOD for the detection of influenza virus (H1N1) in ultrapure water

391 is 0.25 pg/mL, while the LOD in human serum was evaluated to be 0.9 pg/mL. A

392 comparison of the obtained LODs with other detection systems indicated that

393 this developed system has a comparable sensitivity (Table 1) [48-53].

394   Furthermore, by analyzing the kinetics of the detection cycle of the time-course

395   change in the FL intensity of gCNQDs (Fig. S6 in Supplementary data), it can be

396   observed that the FL enhancement occurred rapidly when the target virus was

397   introduced to the 96 well-plate reaction chamber that allowed rapid

398   fluorescence detection up to 5 min after which no major FL modifications had

399   been observed up to 10 min and above after this optimum point. The detection

400   protocol was expedited for influenza virus (H1N1) detection in a matter of ~5

401   min even in clinical samples containing target influenza virus. Hence, this

402   developed detection platform could achieve faster results for urgent diagnostic

403   measures better than or replace commercial rapid diagnostic kits, which requires

404   ~15 − 20 min, and/or (qRT-PCR), which requires several hours (4 − 6 h) for

405   detection, such that point-of-care testing could be expected if this detection

406   protocol is fully integrated with portable instrumentation system. Moreover, it is

407   plausible to point out that this detection platform can be tuned appropriately to

408   detect other target viruses.

409   *3.5. Specific recognition of influenza virus (H1N1)*

410   To verify the specificity and selective disposition of the developed immunosensor

411   towards influenza virus (H1N1) as the target virus, some other viruses such as

412   Zika virus, NoV-LPs, HEV-LPs, Dengue were employed to study the potential

413   interferences that may be exhibited by monitoring the response of the

414   fluoroimmunosensors in the presence of ~ 10 ng/mL other viruses. As shown in

415   Fig. 5, the specificity of H1N1 is proved by the marked difference in the induced

change in the FL intensity of the fluoroimmunosensor signals compared to other non-specific viruses which exhibited very negligibly change in signals. It is pertinent to state here, that the specificity of the fluoroimmunosensor is mainly dependent on the antibodies involved in the immuno-reactions. The specific affinity of the influenza virus to be confined in core-satellite system with the specific Ab-conjugated nanomaterials resulted in the substantial selectivity of the developed biosensor. In addition, to highlight the contributions of gCNQD's surface chemistry to the immunoassay specificity and sensitivity, it is appropriate to stress that hemagglutinin (HA), a major envelope of influenza A virus glycoprotein is composed of HA1 (positively charged), HA2 and signal peptides [54]. Nonetheless, the protein-associated amino acids in the influenza A virus may exhibit a general charge-neutrality at physiological pH [55]. Therefore, electrostatic interaction / repulsion effects are minimized between the influenza A virus and gCNQDs (-18.1 mV) or Ab-gCNQDs (-23.5 mV) (Fig. S3 in Supplementary data). It can therefore be inferred that the influenza A virus' avidity towards the antibody-conjugated gCNQDs / MP-MoO$_3$ QDs resulted in the immunoreactions leading to the specific and sensitive virus detection.

3.6. Detection of clinically isolated influenza virus (H3N2 RNA) and comparison with a commercial test kit.

437   In order to boost the analytical figures of merit of our novel detection system,

438   clinically isolated influenza virus A/Yokohama/110/2009 (H3N2) was tested

439   using the Ab-(H3N2)-conjugated MP-MO$_3$ QDs. The specimen sample containing

440   known PFU/mL of influenza virus (H3N2 RNA) was subjected to biosensing

441   detection within the range of 45 – 25,000 PFU/mL, which triggered the FL

442   enhancement of the probe (Fig. 6A and B). The LOD was evaluated to be 45

443   PFU/mL. The performance of developed fluoroimmunoassay was further

444   evaluated against a commercial rapid influenza diagnostic kit (RIDT) – *QuikNavi-*

445   *Flu* 2 (Denka Seiken Co. Ltd, Tokyo, Japan). For the RIDT, the concentration of

446   <5000 PFU/mL of the clinically isolated influenza virus A/Yokohama/110/2009

447   (H3N2) could not be detected (Fig. S7). Whereas our developed system is

448   responsive to the virus level up to 45 PFU/mL. This result indicates that our

449   sensing strategy is ~100 times as sensitive as the commercial RIDT. However, it is

450   pertinent to point that both detection techniques are quite different in principle

451   and the development of a rapid diagnostic kit with our designed system may

452   significantly improve the sensitive detection of influenza virus.

453

454   **4. Conclusion**

455   A novel combination of graphitic carbon nitride and molybdenum-based QDs

456   was deployed for the fluoroimmunoassay of influenza virus. The sensitivity

457   achieved herein for influenza virus detection was 0.25 pg/mL in DI water and

458   0.9 pg/mL in human serum. In a clinical sample, influenza virus A (H3N2) was

459 detected using this assay with LOD of 45 PFU/mL within a linear dynamic

460 detection range of 45 – 25,000 PFU/mL. The assay showed a good sensitivity for

461 the detection of influenza virus in samples with complex matrices owing to the

462 magnetic separation/purification protocol of the assay. This work shows that the

463 nanoparticles combination can be adopted as potential materials for constructing

464 efficient platforms for virus detection. In addition, they are highly competitive

465 and low cost alternatives deployable for the plasmonic-induced and optical

466 detection of infectious viral biomolecules by using the desired antigen-antibody

467 pair to devise a vast pool of biosensors to meet the demand for speedy and

468 responsive assessment assays.

469

479

Appendix A. Supplementary data

Supplementary material related to this article can be found, in the online version, at doi:…

References

[1] World Health Organization (WHO), Coronavirus disease 2019 (COVID-19) Situation Report–24, Feb. 13. 2020 (adapted from: https://www.who.int/emergencies/diseases/novel-coronavirus-2019/situation-reports).

[2] O.J. Achadu, T. Nyokong, *In situ* one-pot synthesis of graphitic carbon nitride quantum dots and its 2, 2, 6, 6-tetramethyl (piperidin-1-yl) oxyl derivatives as fluorescent nanoprobes for ascorbic acid, Anal. Chim. Acta. 991 (2017) 113–126.

[3] S. Benítez-Martínez, M. Valcárcel, Graphene quantum dots in analytical science, Trends Anal. Chem. 72 (2015) 93-113.

[4] Y. Dong, Q. Wang, H. Wu, Y. Chen, C. H. Lu, Y. Chi, H. H. Yang, Graphitic carbon nitride materials: sensing, imaging and therapy, Small 12 (2015) 5376–5393.

[5] H. Li, F.Q. Shao, H. Huang, J.J. Feng, A.J. Wang, Eco-friendly and rapid microwave synthesis of green fluorescent graphitic carbon nitride

500 quantum dots for vitro bioimaging, *Sens.* Actuators B Chem.

501 226 (2016) 506-511.

502 [6] Y.L. T. Ngo, W.M. Choi, J.S. Chung, S.H. Hur, Highly biocompatible

503 phenylboronic acid-functionalized graphitic carbon nitride quantum dots for

504 the selective glucose sensor, Sens Actuators B Chem. 282 (2019) 36-44.

505 [7] S. Zhu, Y. Song, X. Zhao, J. Shao, J. Zhang, B. Yang, The photoluminescence

506 mechanism in carbon dots (graphene quantum dots, carbon nanodots, and

507 polymer dots): current state and future perspective, Nano Res. 8 (2015) 355-

508 381.

509 [8] S. Barman, M. Sadhukhan, Facile bulk production of highly blue fluorescent

510 graphitic carbon nitride quantum dots and their application as highly

511 selective and sensitive sensors for the detection of mercuric and iodide ions

512 in aqueous media, J. Mater. Chem. 22 (2012) 21832–21837.

513 [9] X. Pang, H. Bian, W. Wang, C. Liu, M. S. Khan, Q. Wang, J. Qi, Q. Wei, B.

514 Du, A bio-chemical application of N-GQDs and g-C3N4 QDs sensitized TiO2

515 nanopillars for the quantitative detection of pcDNA3-HBV, Biosens.

516 Bioelectron. 91 (2017) 456-464.

517 [10] B. Sun, J. Dong, L. Cui, T. Feng, J. Zhu, X. Liu, S. Ai, A dual signal-on

518 photoelectrochemical immunosensor for sensitively detecting target avian

519 viruses based on AuNPs/g-C_3N_4 coupling with CdTe quantum dots and *in*

520 *situ* enzymatic generation of electron donor, Biosens. Bioelectron. 124-125

521 (2019) 1-7.

522 [11]M. Y. Xiong, Q. M. Rong, H. M. Meng, X. B. Zhang, Two-dimensional

523   graphitic carbon nitride nanosheets for biosensing applications, Biosens.

524   Bioelectron. 89 (2017) 212–223.

525 [12]P. A. Rasheed, T. Radhakrishnan, S. R. Nambiar, R. T. Thomas, N.

526   Sandhyarani, Graphitic carbon nitride as immobilization platform for ssDNA

527   in a genosensor, Sens. Actuators B Chem. 250 (2017) 162.

528 [13]K. Holá, M. Sudolská, S. Kalytchuk, D. Nachtigallová, A. L. Rogach, M.

529   Otyepka, R. Zbořil, Graphitic Nitrogen Triggers Red Fluorescence in Carbon

530   Dots, ACS Nano. 12 (2017) 12402-12410.

531 [14]C. Li, X. Yang, B. Yang, Y. Yan, Y. Qian, Synthesis and characterization of

532   nitrogen-rich graphitic carbon nitride, Mater. Chem. Phys. 103 (2007) 427-

533   432.

534 [15]X. Zhu, F. Kou, H. Xu, Y. Han, G. Yang, X. Huang, W. Chen, Y. C

535   hi, Z. Lin. Label-free ochratoxin A electrochemical aptasensor based on

536   target-induced non-covalent assembly of peroxidase-like graphitic carbon

537   nitride nanosheets. Sens. Actuators B Chem. 270 (2018) 263-269.

538 [16]T. Han, X. Li, Y. Li, W. Cao, D. Wu, B. Du, Q. Wei, Gold nanoparticles

539   enhanced electrochemiluminescence of graphite-like carbon nitride for the

540   detection of Nuclear Matrix Protein 22, Sens. Actuators B Chemical, 205

541   (2014) 176-183.

542 [17]H. Wang, Q. Zhang, H. Yin, M. Wang, W. Jiang, S. Ai, Photoelectrochemical

543   immunosensor for methylated RNA detection based on g-C_3N_4/CdS quantum

544   dots heterojunction and Phos-tag-biotin, Biosens. Bioelectron. 95 (2017) 124

545   - 130.

546   [18]O. J. Achadu, N. Revaprasadu, Microwave-assisted synthesis of thymine-

547   functionalized graphitic carbon nitride quantum dots as fluorescent

548   nanoprobe for mercury (II), Microchim. Acta. 185 (2018) 461-469.

549   [19]O. J. Achadu, N. Revaprasadu, Tannic acid-derivatized graphitic carbon

550   nitride quantum dots as an "on-off-on" fluorescent nanoprobe for ascorbic

551   acid via copper(II) mediation, Microchim. Acta. 186 (2019) 87-96.

552   [20] H. Tao, T. Hu, J. Yan, J. Di. A comparative study of different

553   reagentless plasmon sensors based on Ag–Au alloy nanoparticles for

554   detection of Hg, Sens. Actuators B Chem. 208 (2015) 43-49.

555   [21]C. Liu, F. Meng, W. Zheng, T. Xue, Z. Jin, Z. Wang, X. Cui,

556   Plasmonic ZnO nanorods/Au substrates for protein microarrays with high

557   sensitivity and broad dynamic range, Sensors Actuators B Chem. 228 (2016)

558   231-236.

559   [22] S. H. Lee, H. Nishi, T. Tatsuma, Tunable plasmon resonance of

560   molybdenum oxide nanoparticles synthesized in non-aqueous media, Chem.

561   Commun. **53** (2017) 12680-12683.

562   [23] X. Lu, R. Wang, F. Yang, W. Iao, W. Liu, L. Hao, X. He, Preparation of

563   MoO_3 QDs through combining intercalation and thermal exfoliation, J.

564   Mater. Chem. C. 4 (2016) 6720-6726.

565   [24] J. Shi, Y. Kuwahara, M. Wen, M. Navlani-Garcia, K. Mori, T. An, H.

566   Yamashita, Room-Temperature and Aqueous-Phase Synthesis of Plasmonic

567   Molybdenum Oxide Nanoparticles for Visible-Light-Enhanced Hydrogen

568   Generation, Chem. Asian J. 11 (2016) 2377 – 2381.

569   [25] S. J. Xiao, X. J. Zhao, P. P. Hu, J. Z. Chu, C. Z. Huang, L. Zhang, Highly

570   Photoluminescent Molybdenum Oxide Quantum Dots: One-Pot Synthesis

571   and Application in 2,4,6-Trinitrotoluene Determination, ACS Appl. Mater.

572   Interfaces. 8 (2016) 8184-8191.

573   [26] H. Yin, Y. Kuwahara, K. Mori, H. Cheng, M. Wen, Y. Huo, H. Yamashita,

574   Localized Surface Plasmon Resonances in Plasmonic Molybdenum Tungsten

575   Oxide Hybrid for Visible-Light-Enhanced Catalytic Reaction, *J. Phys. Chem.*

576   *C.* 42 (2017) 23531-23540.

577   [27] J. Zhang, Y. Pan, Y. Chen, H. Lu, Plasmonic molybdenum trioxide quantum

578   dots with noble metal-comparable surface enhanced Raman scattering, *J.*

579   *Mater. Chem. C.* 6 (2018) 2216-2220.

580   [28] H. Zu, Y. Guo, H. Yang, D. Huang, Z. Liu, Y. Liu, C. Hu, Rapid room-

581   temperature preparation of MoO_{3-x} quantum dots by ultraviolet irradiation

582   for photothermal treatment and glucose detection, New J. Chem. 42 (2018)

583   18533-18540.

584   [29] J. Lee, H. Kim, R. Algar, Thiol-ligand-Catalyzed Quenching and Etching in

585   Mixtures of Colloidal Quantum Dots and Silver Nanoparticles, J. Phys. Chem.

586   C. *121* (2017) 28566-28575.

587   [30] J. K. Vaishnav, T. K. Mukherjee, Long-Range Resonance Coupling-Induced

588   Surface Energy Transfer from CdTe Quantum Dot to Plasmonic Nanoparticle,

589   J. Phys. Chem. C. *122* (2018) 28324-28336.

590   [31]O. Adegoke, M. Morita, T. Kato, M. Ito, T. Suzuki, E.Y. Park, Localized

591   surface plasmon resonance-mediated fluorescence signals in plasmonic

592   nanoparticle-quantum dot hybrids for ultrasensitive Zika virus RNA detection

593   via hairpin hybridization assays, Biosens. Bioelectron. 94 (2017) 513–522.

594   [32] J. Lee, S. R. Ahmed, S. Oh, J. Kim, T. Suzuki, K. Parmar, S. Park, J. Lee, E. Y.

595   Park, A plasmon-assisted fluoro-immunoassay using gold nanoparticle-

596   decorated carbon nanotubes for monitoring the influenza virus, Biosens.

597   Bioelectron. 64 (2015) 311-317.

598   [33] K. Takemura, O. Adegoke, T. Naoto, T. Kato, T. C. Li, N. Kitamoto, T.

599   Tanaka, T. Suzuki, E. Y. Park, Versatility of a localized surface plasmon

600   resonance-based gold nanoparticle-alloyed quantum dot nanobiosensor for

601   immunofluorescence detection of viruses, Biosens. Bioelectron. 89 (2017)

602   998–1005.

603   [34] K. Takemura, J. Lee, T. Suzuki, T. Hara, F. Abe, E. Y. Park, Ultrasensitive

604   detection of norovirus using a magnetofluoroimmunoassay based on synergic

605   properties of gold/magnetic nanoparticle hybrid nanocomposites and

606   quantum dots, Sens. Actuators B Chem. 296(2019) 126672-126680.

607   [35] F. Nasrin, A. D. Chowdhury, K. Takemura, J. Lee, O. Adegoke, V. K. Deo, F.

608   Abe, T. Suzuki, E. Y. Park, Single-step detection of norovirus tuning localized

609   surface plasmon resonance-induced optical signal between gold nanoparticles

610   and quantum dots, Biosens. Bioelectron. 122 (2018) 16-24.

611   [36] S. R. Ahmed, K. Takemura, T. C. Li, N. Kitamoto, T. Tanaka, T. Suzuki, E. Y.

612   Park, Size-controlled preparation of peroxidase-like graphene-gold

613   nanoparticle hybrids for the visible detection of norovirus-like particles,

614   Biosens. Bioelectron. 87 (2017) 558-565.

615   [37] T. C. Li, Y. Yamakawa, K. Suzuki, M. Tatsumi, M. Razak, T. Uchida, N.

616   Takeda, T. Miyamura, Expression and self-assembly of empty virus-like

617   particles of hepatitis E virus, J. Virol. 71 (1997) 7207-7213.

618   [38] M. Zarei, H. Ahmadzadeh, E. K. Goharshadi, A. Farzaneh, Graphitic carbon

619   nitride embedded hydrogels for enhanced gel electrophoresis, Anal. Chim.

620   Acta 887 (2015) 245-252.

621   [39] K. M. G. Lima, I. M. Raimundo Jr, M. F. Pimentel, Improving the

622   detection limits of near infrared spectroscopy in the determination of

623   aromatic hydrocarbons in water employing a silicone sensing phase, Sens.

624   Actuators B Chem. 125 (2007) 229-233.

625   [40] A. H. Loo, Z. Sofer, D. Bouša, P. Ulbrich, A. Bonanni, M. Pumera,

626   Carboxylic Carbon Quantum Dots as a Fluorescent Sensing Platform for DNA

627   Detection, ACS Appl. Mater. Interfaces, 8 (2016) 1951−1957.

628   [41] Y. Zhou, K.J. Mintz, S. K. Sharma, R. M. Leblanc, Carbon Dots: Diverse

629   Preparation, Application, and Perspective in Surface Chemistry, Langmuir, 35

630   (2019) 9115-9132.

631   [42] H. Ding, S. B. Yu, J. S. Wei, H. M. Xiong, Full-Color Light-Emitting Carbon

632   Dots with a Surface-State-Controlled Luminescence Mechanism, ACS Nano 10

633   (2016) 484-91.

634 [43] F. Yuan, Z. Wang, X. Li, Y. Li, Z. Tan, L. Fan, S. Yang, Bright Multicolor

635 Band-gap Fluorescent Carbon Quantum Dots for Electroluminescent

636 Light-Emitting Diodes, Adv. Mater. 29 (2017) 1604436-1604442.

637 [44] S. Y. Gu, C. T. Hsieh, Y. A. Gandomi, J. K. Chang, J. Li, J. L. Li, H. A. Zhang,

638 Q. Guo, K. C. Lau, R. Pandey, Microwave Growth and Tunable

639 Photoluminescence of Nitrogen-doped Graphene and Carbon Nitride

640 Quantum Dot, J. Mater. Chem. C 7 (2019) 5468-5476.

641 [45] J. Wang, S. Cao, Y. Ding, F. Ma, W. Lu, M. Sun, Theoretical Investigations

642 of Optical Origins of Fluorescent Graphene Quantum Dots, Sci. Rep. 6

643 (2016) 24850-24855.

644 [46] E.G.C. Neiva, M.F. Bergamini, M.M. Oliveira, L.H. Marcolino, A.J.G.

645 Zarbin, PVP-capped nickel nanoparticles: synthesis, characterization and

646 utilization as a glycerol electrosensor, Sens. Actuators B Chem. 196 (2014)

647 574-581, 10.1016/j.snb.2014.02.041

648 [47] A. Plácido, C. Pereira, A. Guedes, M. F. Barroso, R. Miranda-Castro, N. D.

649 Santos-Álvarez, C. Delerue-Matos, Electrochemical genoassays on gold-

650 coated magnetic nanoparticles to quantify genetically modified organisms

651 (GMOs) in food and feed as GMO percentage, Biosens. Bioelectron. 110

652 (2018) 147-154.

653 [48] Chang, Y.F., Wang, S.F., Huang, J.C., Su, L.C., Yao, L., Li, Y.C., Wu, S.C.,

654 Chen, Y.M., Hsieh, J.P., Chou, C., Detection of swine-origin influenza A

655 (H1N1) viruses using a localized surface plasmon coupled fluorescence fiber-

656 optic biosensor. 2010. Biosens. Bioelectron. 26, 1068–1073.

657 [49] J. Lee, K. Takemura, E. Y. Park, Plasmonic/magnetic graphene-based

658 magnetofluoro-immunosensing platform for virus detection, Sens. Actuators,

659 B Chem. 276 (2018) 254-261.

660 [50] Y. Li, M. Hong, B. Qiu, Z. Lin, Y. Chen, Z. Cai, G. Chen, Highly sensitive

661 fluorescent immunosensor for detection of influenza virus based on Ag

662 autocatalysis, Biosens. Bioelectron. 54 (2014) 358-364.

663 [51] U. Jarocka, R. Sawicka, A. Góra-Sochacka, A. Sirko, W. Zagórski-Ostoja, J.

664 Radecki, H. Radecka, Electrochemical immunosensor for detection of

665 antibodies against influenza A virus H5N1 in hen serum, *Biosens. Bioelectron.*

666 *55* (2014) 301–306.

667 [52] S. R. Ahmed, M. A. Hossain, J. Y. Park, S. H. Kim, D. Lee, T. Suzuki, J. Lee, E.

668 Y. Park, Metal enhanced fluorescence on nanoporous gold leaf-based assay

669 platform for virus detection. 2014. Biosens. Bioelectron. 58 (2014) 33-39.

670 [53] S. R. Ahmed, S.R., J. Kim, T. Suzuki, J. Lee, E. Y. Park, Detection of influenza

671 virus using peroxidase-mimic of gold nanoparticles, Biotechnol. Bioeng. 113

672 (2016) 2298-2303.

673 [54] N. Arinaminpathy., B. Grenfell, Dynamics of Glycoprotein Charge in the

674 Evolutionary History of Human Influenza. PLoS One. 5 (2010) 1–7.

675 https://doi.org/10.1371/journal.pone.0015674.

676 [55] Y. Kobayashi, Y. Suzuki, Compensatory Evolution of Net-Charge in

677 Influenza A Virus Hemagglutinin. PLoS One. 7 (2012).

678 https://doi.org/10.1371/journal.pone.0040422.

679

680   **Table 1.** A comparison of some recent reports/results on influenza virus detection

681   systems.

Method of detection	Target virus	LOD	Ref.
Fluorescence fiber-optic biosensor	H1N1	13.9 pg/mL	[48]
Magnetofluoro-immunoassay	H1N1	6.07 pg/mL	[49]
Ag-S covalent labelling	H1N1	0.1 pg/mL	[50]
Electrochemical immunosensor	H5N1	2.1 pg/mL	[51]
Metal-enhanced fluoroimmunoassay	H1N1	1 ng/mL	[52]
Peroxidase mimic	H1N1	10 pg/mL	[53]
Magnetoplasmonic fluoroimmunoassay	H1N1	0.25 pg/mL (DI water) and 0.9 pg/mL (in serum)	This work

682

683

686
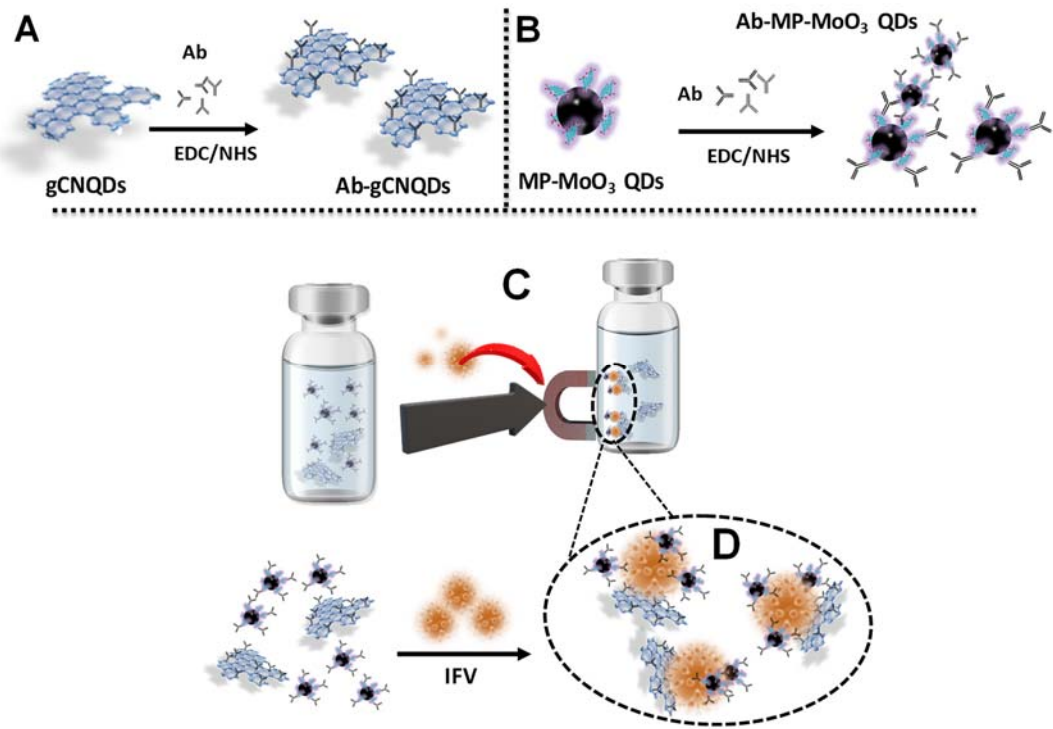
Scheme 1. (A) Antibody conjugation to gCNQDs via EDC/NHS chemistry. (B) Antibody conjugation to MP-MoO$_3$ QDs via EDC/NHS chemistry. (C) Magnetic separation and purification step upon target virus addition (D) Core-satellite immunocomplex of gCNQDs and MP-MoO$_3$ QDs in the presence of influenza virus.

692
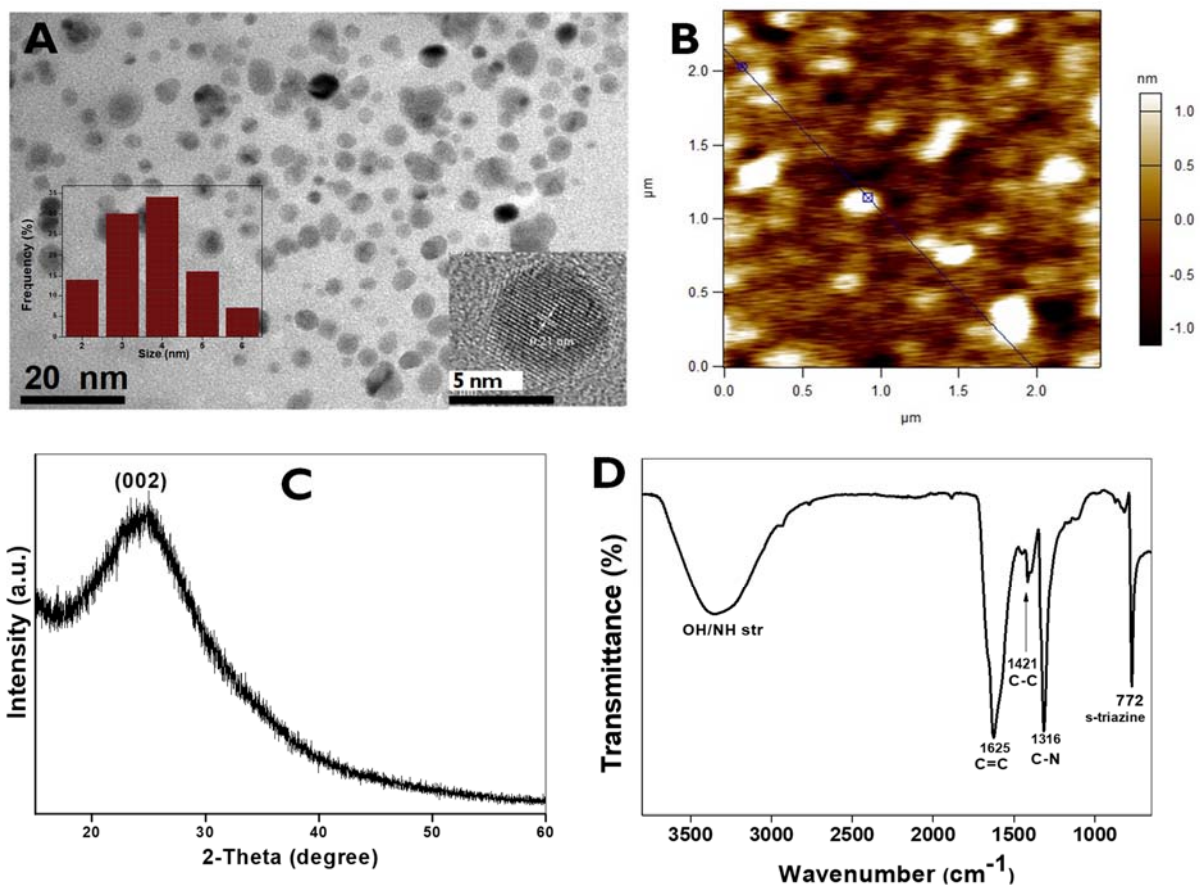
693

694

695   Fig. 1. Characterization results of gCNQDs showing (A) TEM image (inset HR-

696   TEM). (B) AFM (C) XRD pattern and (D) FTIR spectra.

697

698

699

700
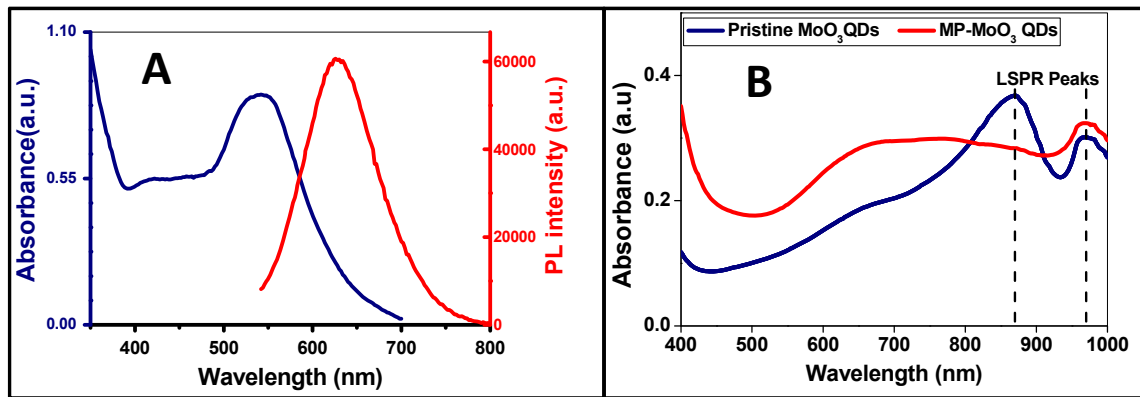
Fig. 2. (A) UV-vis and FL emission of gCNQDs. (B) The UV-vis absorption spectra

of MoO₃ QDs and their magnetic derivative. Solvent: ultrapure water. $\lambda_{ex(gCNQDs)}$

= 500 nm.

704
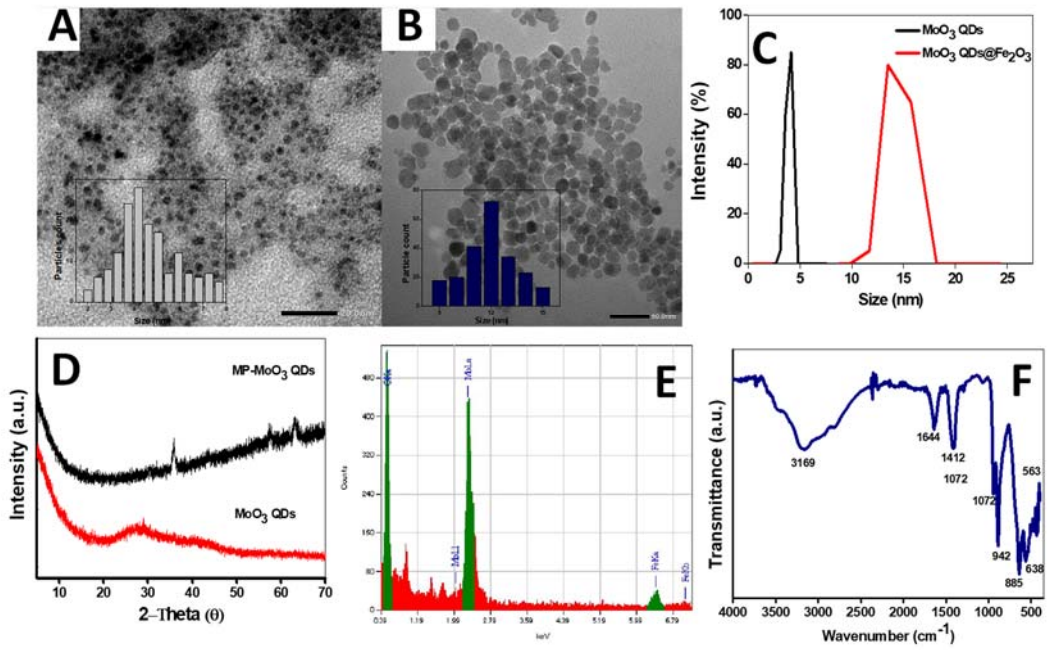
708   Fig. 3. Characterization of MP-MoO₃ QDs showing (A) TEM image of pristine

709   MoO₃ QDs (B) TEM of magnetoplasmonic MoO₃ QDs. (C) DLS, (D) XRD

710   patterns, (E) EDX and (F) FTIR spectra.

711

712
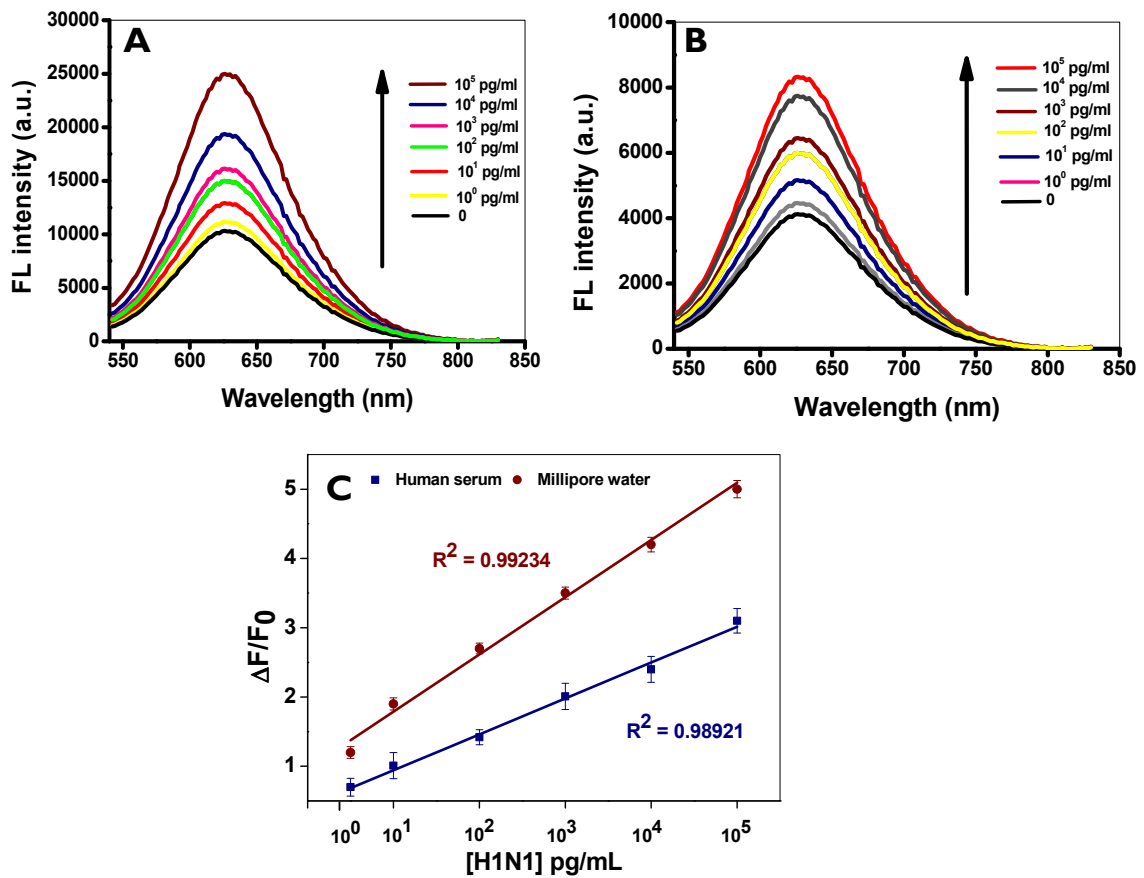
Fig. 4. H1N1 detection via enhancement of the FL emission of gCNQDs

measured in ultrapure water (A) or human serum (B) and their calibration plots

(C). λ_{ex} = 500 nm.

716

717
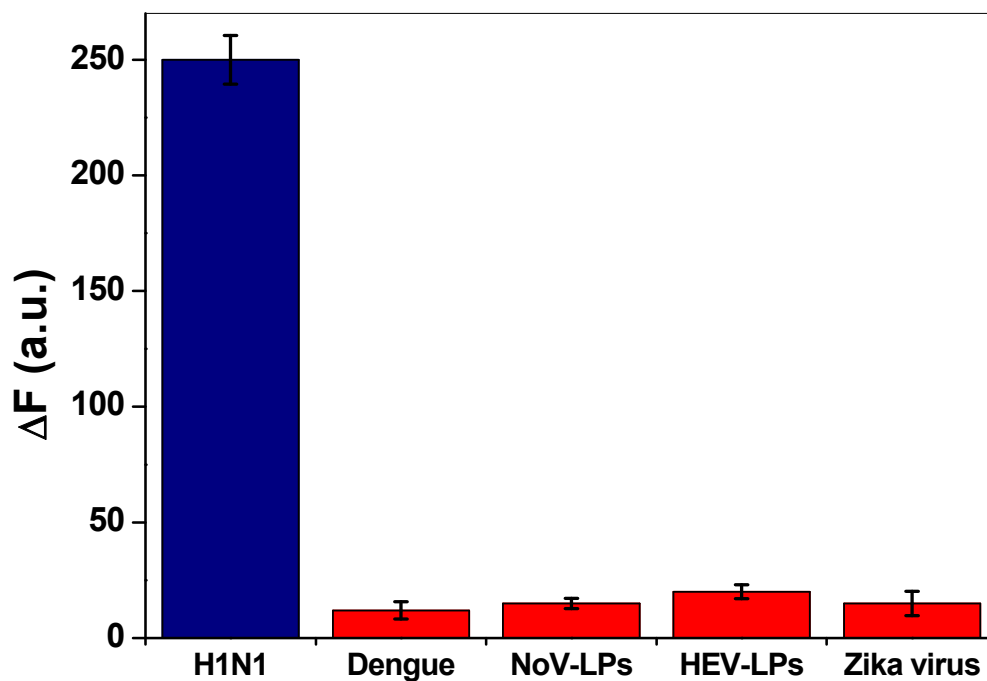
Fig. 5. The selectivity result of gCNQDs/MP-MoO$_3$ QDs-based

fluoroimmunosensor for influenza A/H1N1 detection in the presence of 10 ng/mL

of other virus/VLPs and 10^3 PFU/mL of H3N2 as negative control.

721
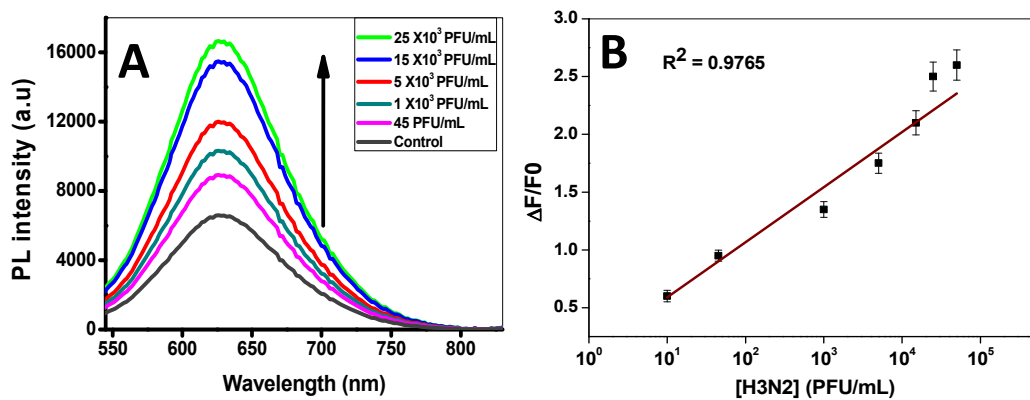
722

723 Fig. 6. (A) FL emission spectra of gCNQDs showing the detection of clinically

724 isolated influenza virus RNA (H3N2) and (B) the corresponding H3N2 detection

725 calibration plot within the linear range. λ_{ex} = 500 nm.

726
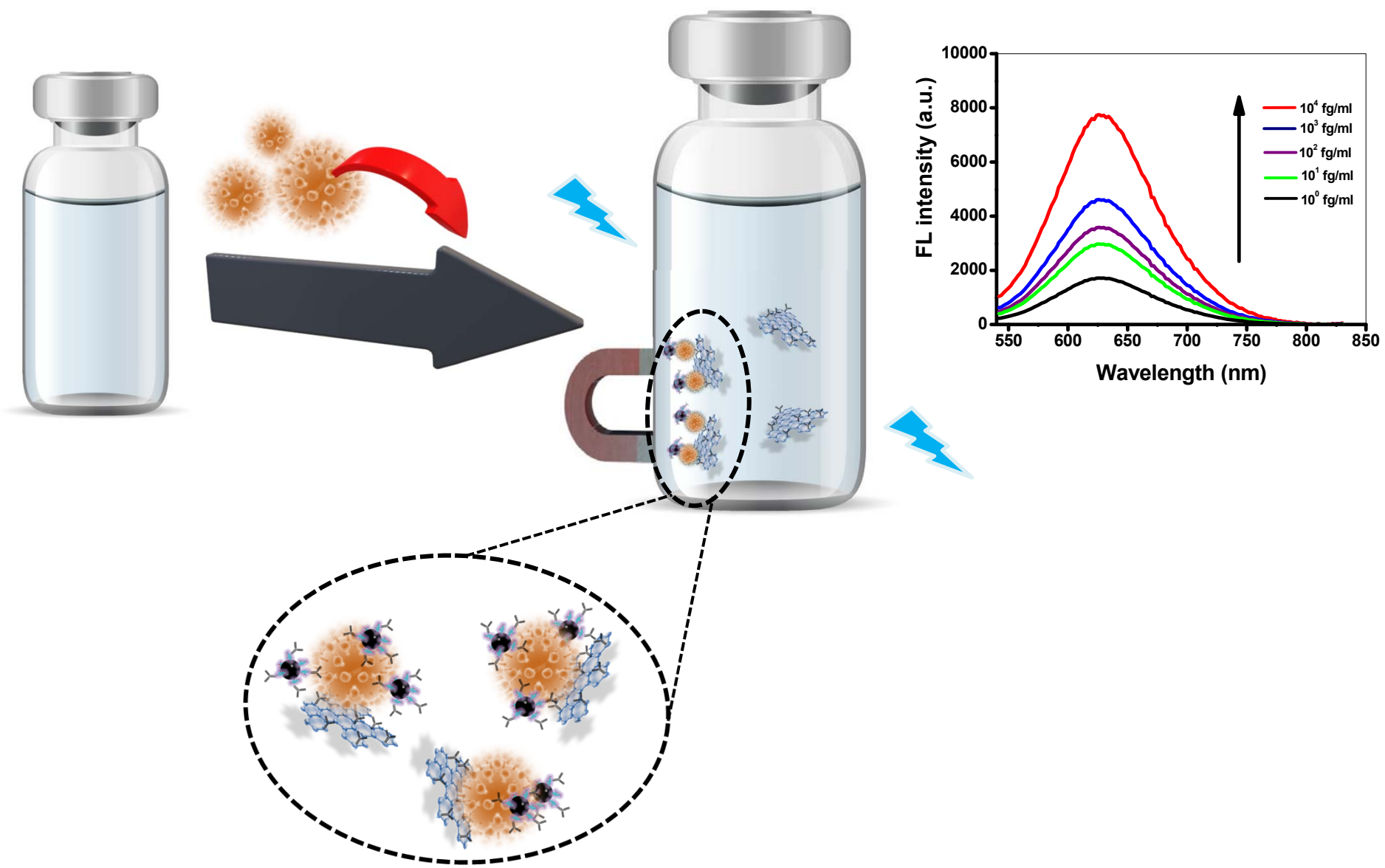
Supplementary Data

Plasmonic/magnetic molybdenum trioxide and graphitic carbon nitride quantum dots-based fluoroimmunosensing system for influenza virus

Ojodomo J. Achadu[a], Kenshin Takemura[b], Indra Memdi Khoris[b], Enoch Y. Park[a,b,*]

[a] *Research Institute of Green Science and Technology, Shizuoka University, 836 Ohya Suruga-ku, Shizuoka 422-8529, Japan*

[b] *Laboratory of Biotechnology, Department of Bioscience, Graduate School of Science and Technology, Shizuoka University, 836 Ohya Suruga-ku, Shizuoka 422-8529, Japan*

E-mail:
ojodomo.john.achadu@shizuoka.ac.jp (OJA)
takemura.kenshin.16@shizuoka.ac.jp (KT)
indra.memdi.khoris.17@shizuoka.ac.jp (IMK)
park.enoch@shizuoka.ac.jp (EYP)

---

[*] Corresponding author:
E-mail address: park.enoch@shizuoka.ac.jp (E.Y. Park). Tel (Fax): +81-54-238-4887

Fig. S1. Overlay of the UV-Vis spectra of MP-MoO$_3$ QDs and the FL of gCNQDs. λ_{exc} = 500 nm. Solvent: PBS (7.6).
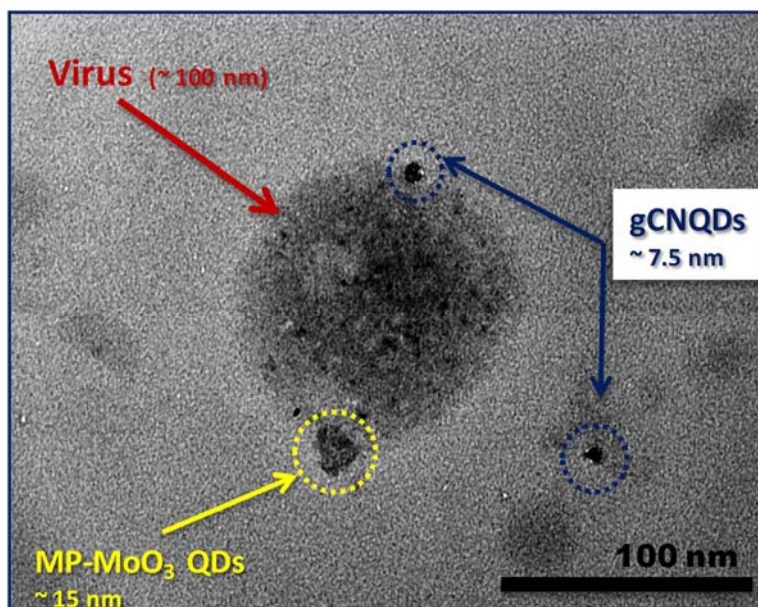
Fig. S2. TEM image of the core-satellite immunocomplex of gCNQDs/Influenza A virus/MP-MoO$_3$ QDs.
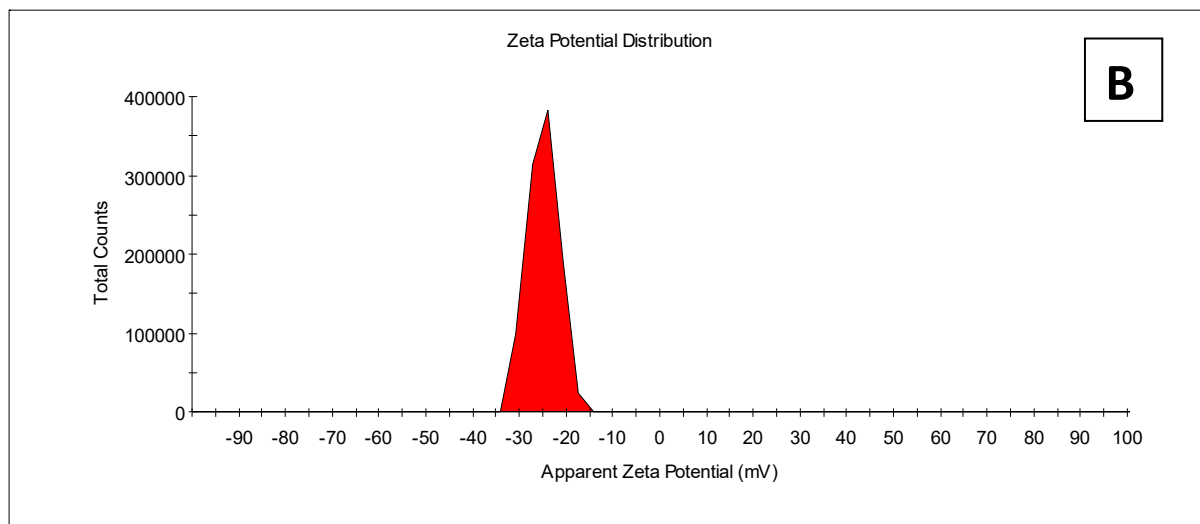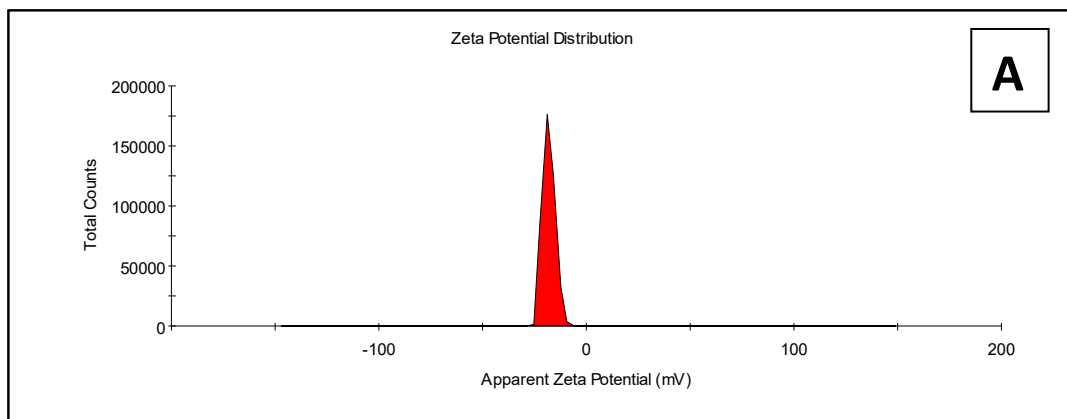
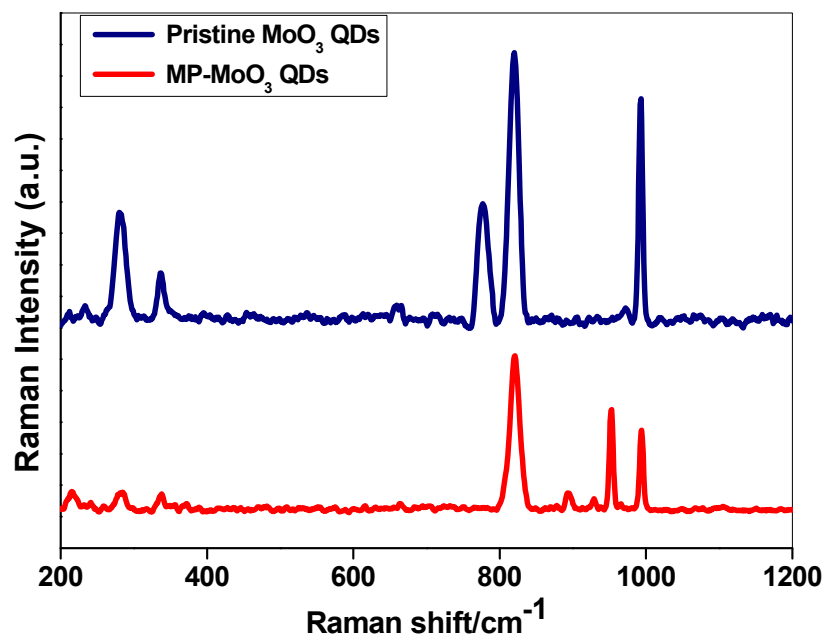**Fig. S3.** Zeta potential results (**A**) gCNQDs, and (**B**) antibody-conjugated gCNQDs.

Fig. S4. Raman spectra of MP-MoO₃ QDs and the magnetic derivatized MP-MoO₃ QDs.
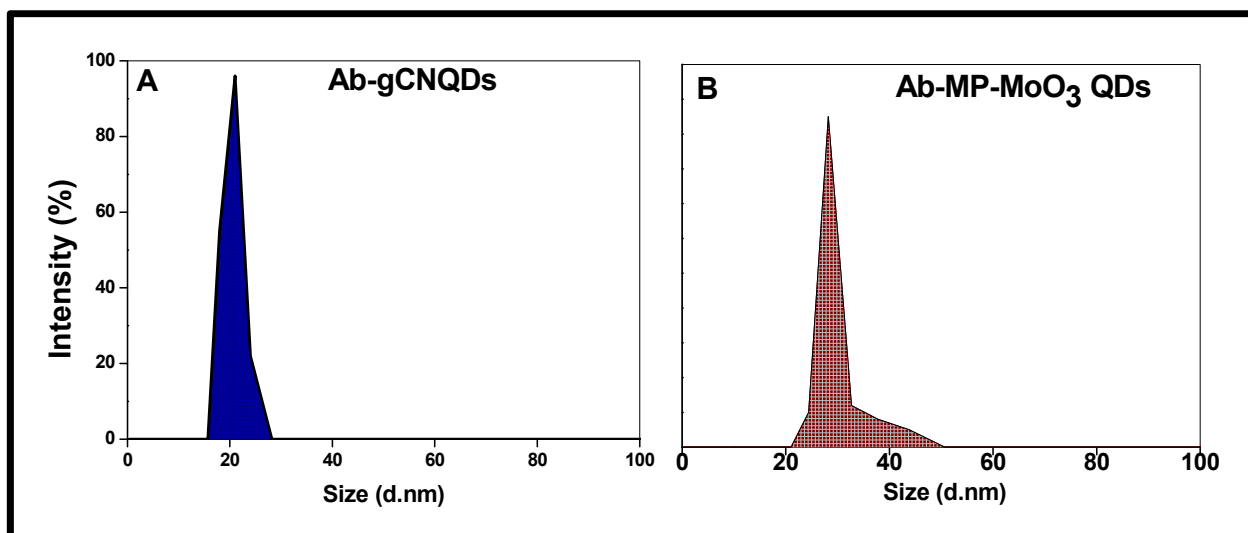
Fig. S5. DLS results of the antibody conjugated materials showing their respective hydrodynamic sizes (**A**) antibody-gCNQDs, (**B**) antibody-MP-MoO₃ QDs.
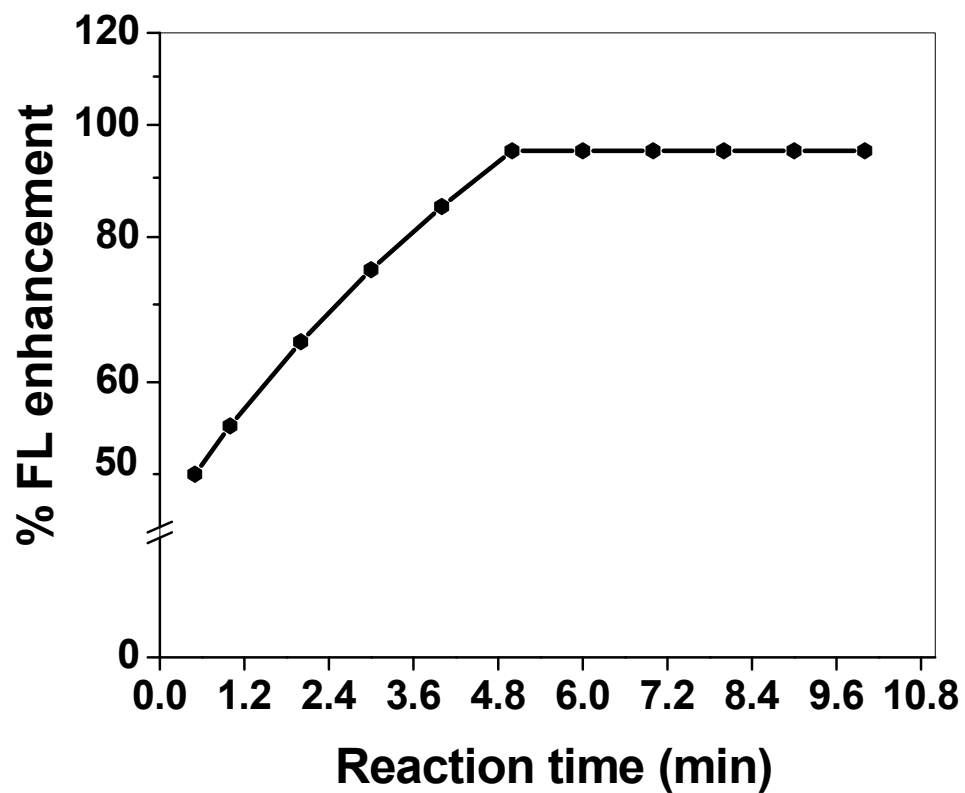
Fig. S6. Time course fluorescence intensity change against reaction time showing the completion of the reaction in ~5 min.

Fig. S7. Influenza virus A/Yokohama/110/2009 (H3N2) detection using commercial RIDT. A, B, and C denote influenza A virus, influenza B virus, and control, respectively.

Fluorescence quantum yield (Φ_F) deteremination

Fluorescence quantum yields of the GQDs were determined by the comparative method [1], equation 1.

$$\Phi_F = \Phi_{F(Std)}\frac{F.A_{Std}.n^2}{F_{Std}.A.n^2_{Std}} \qquad (1)$$

Where A and A_{Std} are the absorbances of the sample and the standard at the excitation wavelength, respectively. F and F_{Std} are the areas under the fluorescence curves of the GQDs and the standard, respectively and n and n_{Std} are the refractive indices of the solvent used for the sample and standard, respectively. Rhodamine 6G in ethanol (Φ_F = 0.94 [2]) was used as the standard.

References

1. Fery-Forgues S, Lavabre D (1999) Are fluorescence quantum yields so tricky to measure? A demonstration using familiar stationery products. J Chem Ed. 76:12660-1264.
2. Fischer S, Georges J (1996) Fluorescence quantum yield of Rhodamine 6G in ethanol as a function of concentration using lens spectrometry. Chemical physics letters. 260:115-118.